Engineering Structures 321 (2024) 118930

Contents lists available at ScienceDirect

Engineering Structures

journal homepage: www.elsevier.com/locate/engstruct

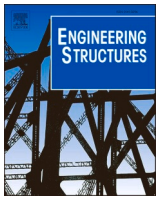

Experimental study on the behaviour of austenitic stainless steel and carbon steel welded shear connectors

R. Presswood [a,*], S. Afshan [a], F. Meza [b], N. Baddoo [b], M. Shaheen [c], P. Desnerck [d]

[a] Faculty of Engineering and Physical Sciences, University of Southampton, United Kingdom
[b] The Steel Construction Institute, United Kingdom
[c] School of Architecture, Building and Civil Engineering, Loughborough University, United Kingdom
[d] Department of Engineering, University of Cambridge, United Kingdom

ARTICLE INFO

Keywords:
Composite beam
Push-out tests
Shear connector
Stainless steel
Welded stud

ABSTRACT

Steel-concrete composite beams are commonly used in bridge construction. The corrosion of the supporting steel beams is known to be a cause of deterioration of composite bridges, while the shear connectors may also be at risk of corrosion from chlorides migrating through cracks in the concrete deck. Stainless steel composite beams offer a viable solution to the steel corrosion problem in harsh environments. However, their design is outside the scope of the current international design standards due to a lack of reliable experimental data. This paper investigates the structural behaviour of austenitic EN 1.4301 stainless steel and carbon steel shear studs welded to lean duplex EN 1.4162 I-section beams, focusing on the strength, ductility and the weld quality of the studs. Material tests were conducted on the studs and welded connection, with weld quality examined through X-ray computerised tomography (CT) scanning and etching. The paper also presents the results from eight push-out tests, assessing the shear stud resistance predicted by existing international design codes for steel-concrete composite construction. In particular, the European and U.S. bridge design codes were found to give safe-sided shear resistance predictions for the austenitic stainless steel studs welded onto lean duplex beams, which performed comparably to literature test results on carbon steel studs welded to carbon steel beams. However, the carbon steel studs could not be successfully stud welded to lean duplex stainless steel beams, thus their use is not recommended in lean duplex stainless steel composite beams. It is the authors' intention that the results presented herein will contribute to the development of the design rules for shear connectors needed for the European and U.S. design codes for duplex stainless steel composite bridges.

1. Introduction

Steel-concrete composite beams have been widely used in bridge construction since the early 20th Century. They offer rapid construction, material efficiency, versatility and enable shallower deck, resulting in weight savings and aesthetic improvements. In composite bridges, the girders are typically formed of carbon steel, which is economical, versatile, widely available and familiar to structural engineers. However, carbon steel is highly susceptible to corrosion, requiring initial coating and ongoing maintenance to prevent deterioration of the steelwork, which can have a significant impact on the life cycle cost of the bridge. Corrosion is more critical for bridges near coastal areas or spanning roads where de-icing salts are used.

The design of bridge decks differs in the U.S. and Europe, with cracking of the concrete slab down to the rebars, and sometimes through the concrete slab, being more likely with the U.S. design approach than with the European approach. This and the use of Calcium or Magnesium Chloride (CaCl or MgCl) de-icing salts, which diffuse through concrete at a faster rate than the more commonly used Sodium Chloride (NaCl) de-icing salts, has created some concerns on the susceptibility of shear studs to corrosive attack.

The use of duplex stainless steel for the main girders of a composite bridge has recently gained attention owing to its excellent corrosion resistance. Life cycle cost studies have shown that despite the higher initial material costs, using duplex stainless steel for the steelwork can lead to a more economical solution compared to traditional painted carbon steel due to the avoidance of the need to repaint the steelwork [1, 2]. The duplex grades, and in particular the less-alloyed lean duplex, are

* Corresponding author.
E-mail address: r.s.presswood@soton.ac.uk (R. Presswood).

https://doi.org/10.1016/j.engstruct.2024.118930
Received 26 April 2024; Received in revised form 6 August 2024; Accepted 3 September 2024
Available online 19 September 2024

preferred over the austenitic grades for their high strength. Compared to weathering steels which show satisfactory performance under normal atmospheric conditions, stainless steel girders are capable of withstanding corrosion in harsh service environments where the material comes into contact with salt water, or where high concentrations of chlorides are present in the air or where de-icing salts are of a concern [1,3]. Stainless steel also has good sustainability credentials, with 95 % of it currently being recycled at end of life, and the average recycled content of new stainless steels standing at 85 % in Europe [4]. More than 30 bridges have been constructed using duplex stainless steels over recent years, including the new road bridge at Pooley Bridge in the UK, pedestrian bridges in the towns of Haro and Aguilas in Spain, and railway bridges in Stockholm. In-service inspections of eleven duplex stainless steel bridges in Europe carried out in 2015/16 demonstrated that duplex stainless steel is a highly durable material choice for bridge structural elements in salty atmospheres in coastal locations or where risks exist from use of de-icing salt [5]. For further examples see references [6,7].

Welded shear studs are commonly used in composite bridges for their rapid welding capability through an automatic arc welding procedure. Shear studs also have the benefit that they do not obstruct the concrete slab steel reinforcement and offer equal strength and stiffness against shear stresses in all directions normal to the stud axis [8]. There has been limited research on the use of stainless steel in composite beam construction to date and there is a distinct lack of design guidance for stainless steel-concrete composite beams. The current design rules for carbon steel-concrete composite beams are not directly applicable and need to be verified on the basis of relevant structural performance data from experimental testing and numerical modelling analysis.

Amongst the limited research on stainless steel-concrete composite beams are the recent studies by Arrayago et al. [9], Cashell and Baddoo [10], Shamass and Cashell [11] and Zhou et al. [12,13]. Arrayago et al. [9] and Cashell and Baddoo [10] carried out tests on composite slabs with EN 1.4003 ferritic stainless steel decking combined with welded studs and I-section beams made of carbon steel. These studies found that there was no significant difference between the ultimate resistance of the slabs with ferritic stainless steel decking compared to the reference slabs with galvanised steel decking. Shamass and Cashell [11] extended the application of the deformation-based design method, known as the continuous strength method (CSM), originally proposed for carbon steel-concrete composite beams by Gardner et al. [14] to stainless steel composite beams. More recently, Zhou et al. carried out tests on stainless steel-concrete composite beams with welded and bolted shear connectors through push-out tests [12] and full-scale composite beam tests subject to three- and four-point bending [13]. The connectors tested were 16 mm and 19 mm duplex EN 1.4462 fillet welded studs, 16 mm and 20 mm duplex EN 1.4462 stainless steel bolted studs and 16 mm austenitic EN 1.4404 stainless steel bolted studs. The steel beams were UB 180 × 18.1 sections made from austenitic EN 1.4301, duplex EN 1.4462 and lean duplex EN 1.4162 stainless steels. The slab had a depth of 100 mm and the degree of shear connection varied from 0.6 to 1.0. All the tested composite beam specimens exhibited very high ductility under bending, shear and combined bending and shear loads. In the push-out tests, the height to diameter ratio of the studs h/d was found to have more of an effect on stainless steel connectors than carbon steel connectors due to the rounded stress-strain relationship and strain hardening [12]. Based on these tests, Zhou et al. proposed new methods for the design of stainless steel shear connectors [12] and for predicting the moment and shear capacity of stainless steel composite beams [13], similar to the traditional rigid plastic analysis method, but accounting for strain hardening.

The design of steel-concrete composite beams relies on the amount of force the shear connectors are able to transfer between the steel beam and the concrete slab and their ability to exhibit ductile behaviour to ensure an equal distribution of the longitudinal shear force between the studs. Several resistance equations are available in the literature and design standards to determine the shear resistance of stud shear connectors. However, these resistance equations have predominantly been calibrated on the basis of test data for carbon steel studs welded to a carbon steel beam, and therefore, their applicability to stainless steels needs to be investigated. Efforts are currently underway to develop design rules for duplex stainless steel composite bridges in accordance with the design philosophy of the European [15,16] and U.S. [17] design codes. To contribute to this effort, this paper presents an investigation into the structural behaviour of austenitic stainless steel and carbon steel shear studs welded onto lean duplex stainless steel beams. As part of this investigation, eight push-out tests were carried out to characterise the load-slip behaviour of the austenitic stainless steel and carbon steel studs, and assess the current resistance equations for stud shear connectors given in the international standards. The study also included stud tensile coupon tests, stud double shear tests and welded stud tensile tests to investigate the overall quality of the weld between dissimilar metals. It is the authors' intention that the results presented in this paper will contribute to the development of the design rules for shear connectors needed for the development of the European and U.S. design codes for duplex stainless steel composite bridges.

2. Material and weld tests

2.1. Test materials

This section describes the tensile and double shear tests carried out to characterise the nonlinear stress-strain behaviour of the carbon steel and austenitic stainless steel shear studs. The tested shear connectors were carbon steel SD1 and austenitic EN 1.4301 stainless steel SD3 headed studs in accordance with ISO 13918 [18], which are commercially available and can be stud-welded to duplex stainless steel beams. These studs were used in the push-out specimens presented in Section 3. All the tested studs had a diameter of 19 mm and a total height of 150 mm, as shown in Fig. 1**(a)**.

2.2. Stud tensile coupon tests

Tensile coupon tests were conducted to determine the tensile stress-strain behaviour of the shear studs. The studs were machined into proportional coupons with a diameter of 10 mm and a gauge length of 50 mm, as shown in Fig. 1. Two carbon steel SD1 specimens (C1 and C2), and three austenitic EN 1.4301 stainless steel specimens (A1, A2 and A3) were tested. The tests were carried out according to ISO 6892–1 [19] using the test set-up in Fig. 2**(a)**. An Instron electromechanical test machine with 100 kN capacity was used to apply the load at a strain rate of 0.007 % strain/sec up to 2 % strain and then at 0.025 % strain/sec until failure. A 25 mm clip-on extensometer was attached to the central portion of the parallel length to measure the strain. An electrical resistance strain gauge was attached to the centre of each coupon to measure strains up to 2 % strain, Fig. 2**(b)**. Point tracking and 2D digital image correlation (DIC) were used to capture the full strain range of the test specimens. A DIC speckle pattern was applied to one third of the coupon surface area using matte rubber-based paint, and a line of small dots was applied to an adjacent third for point-tracking as shown in Fig. 2**(c)**. A Manta G504B 5MPx camera with a 50 mm lens was set up on either side of the test. One of the cameras was used to capture DIC images and the other camera was used to capture point tracking images. The images were captured at a rate of 0.33 Hz using MatchID Grabber. Fiji ImageJ software was used to process the point tracking images to obtain the strain measurements, while MatchID 2D was used to process the DIC images to obtain longitudinal strain plots. Scribed lines were marked on the original gauge length $L_0 = 50$ mm, given by $5.65\sqrt{A_c}$, where A_c is the coupon cross-sectional area, to enable the measurement of the plastic strain after fracture.

The measured stress-strain responses of the carbon steel and

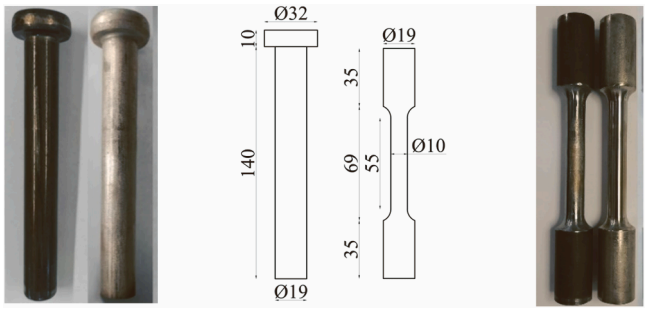

Fig. 1. (a) Left to right: Carbon steel SD1 and austenitic EN 1.4301 stainless steel SD3; (b) Geometry of the headed studs and tensile coupon specimens (dimensions in mm); (c) Photograph of machined tensile coupon specimens.

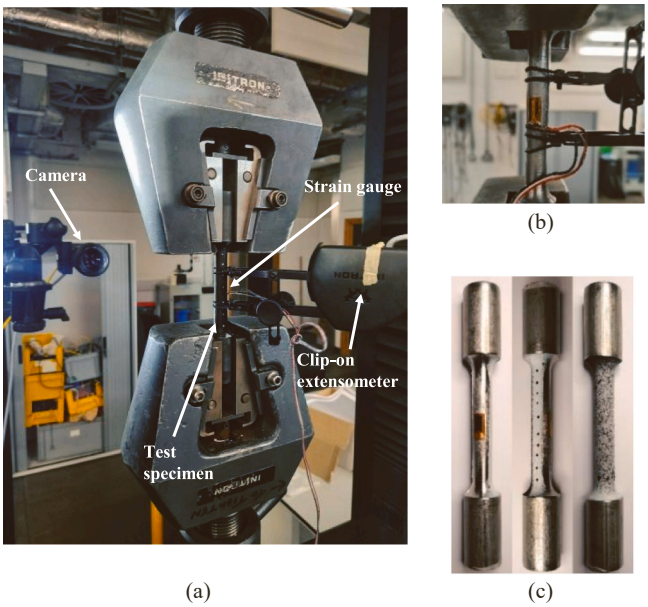

Fig. 2. (a) Experimental setup for tensile tests; (b) Close-up of coupon with extensometer and strain gauge; (c) Strain gauge, point tracking and DIC speckle pattern applied to coupons.

austenitic stainless steel studs are shown in Fig. 3. Table 1 presents the key results, including the Young's Modulus E, 0.2 % proof strength $f_{0.2}$ (defined conventionally as the yield strength), ultimate tensile strength f_u, strain at ultimate tensile strength ε_u and plastic strain at fracture $\varepsilon_{pl,f}$. The Ramberg-Osgood model parameters n and n'_u are also reported in Table 1, which have been calculated according to the method outlined in [20]. The plastic strain at fracture was calculated from $(L_u - L_0)/L_0$, where L_u is the elongated gauge length measured as the distance between the scribed marks by putting the coupon back together after fracture. The Young's Modulus E was determined from a best-fit line fitted to the initial slope of the curve, using the data from the strain gauge since they provide the most accurate strain measurements at low strains, before breaking. All studs failed by ductile fracture in the necked region. The results show that the austenitic stainless steel studs are significantly more ductile than the carbon steel studs, and their ultimate tensile strength is around 40 % higher. Fig. 4 shows the longitudinal strain plots from the DIC just before the coupons fracture, where it can be seen that all the studs exhibited high strains in the necking region. Also, whilst the carbon steel studs showed little strain in the non-necked region, the austenitic stainless steel studs exhibited high strains of 20–50 %.

2.3. Stud double shear tests

Double shear tests were performed to measure the shear load-slip responses of the studs. Assuming the behaviour of the welded metal is similar to the stud material, the deformation of the stud obtained from these tests can be regarded as a lower bound of the slip expected for a shear stud connector, in which the concrete slab does not allow for any bending of the stud. The tests were conducted on 10 mm diameter specimens which were machined from the shank of the headed studs, with dimensions shown in Fig. 5**(a)**. The ends of the specimens were threaded to allow a nut to be tightened on each end. Two tests were performed on the carbon steel (S-C1 and S-C2) and austenitic stainless steel EN 1.4301 (S-A1 and S-A2) studs. The specimens before testing are shown in Fig. 5**(a)**. The nuts were hand tightened to prevent lateral movement of the specimen or plates, while ensuring that no preload was applied. The shear plates were machined from high strength EN 24 steel with a minimum specified yield strength of 680 MPa to ensure that the plates did not deform plastically during the test. The holes in the plates were of 12 mm diameter. Tests were carried out in a Schenck 630 kN servo-hydraulic testing machine using displacement control at a rate of 0.01 mm/sec. Point tracking was used to measure the relative displacements of the plates at the location of the rod specimens, without

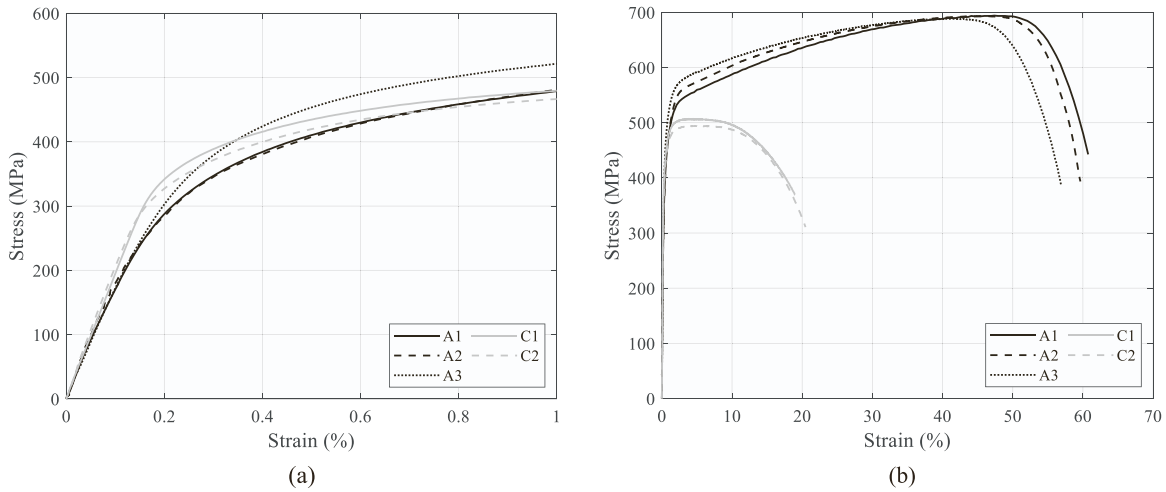

Fig. 3. Measured tensile stress-strain responses of carbon and austenitic stainless steel studs; (a) small strain range; (b) full strain range.

Table 1
Summary of key tensile material properties.

Material	Specimen	E (MPa)	$f_{0.2}$ (MPa)	f_u (MPa)	ε_u (%)	$\varepsilon_{pl,f}$ (%)	n	n'_u
Carbon Steel	C1	203,000	417	506	5.3	18.6	8.93	6.39
	C2	212,000	398	494	5.9	20.3	7.53	8.33
	Mean	207,500	408	500	5.6	19.5	8.23	7.36
Austenitic EN 1.4301	A1	190,000	387	694	47.4	61.3	4.50	4.18
	A2	195,000	379	693	45.2	60.0	4.63	4.95
	A3	194,000	429	688	41.8	54.2	4.14	4.47
	Mean	193,000	398	692	44.8	58.5	4.42	4.53

capturing spurious deformations of the machine. The plates were painted black and small white dots were added. The test setup is shown in Fig. 5**(b)**. A Manta G504B 5MPx camera with a 105 mm lens was set up in front of the test specimen. MatchID Grabber was used to capture images at a rate of 0.33 Hz, and Fiji ImageJ software was used to process the images to obtain displacements of the individual dots.

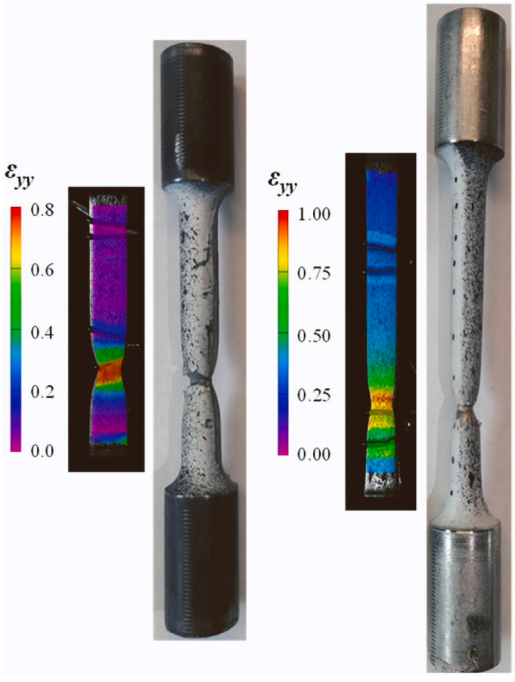

Fig. 4. Plots of longitudinal strain ε_{yy} from DIC just before coupon fracture, left to right: C1 and A3.

The results of the double shear tests in terms of the load per shear plane (i.e. half the applied total load) and the slip (i.e. relative displacement of the middle plate) together with the double section shear failure modes are shown in Fig. 6. The ductility of the austenitic stainless steel studs subject to a shear force is clearly superior to that of the carbon steel studs. The key test results are summarised in Table 2, where k is the initial stiffness, $F_{v,u}$ is the peak load, d_u is the displacement at the peak load and d_f is the displacement at fracture. The results show good repeatability, although there is some variation in the displacement at which fracture occurs and the steepness of the fracture slope. The slight differences between the repeat tests could be due to the hand tightening of nuts at either side which may have affected the stiffness of the test results, and also induced some slight bending in the rod specimens. Nevertheless, there is good overall agreement between the slope, strain hardening, peak load and displacement at fracture for each pair of tests. Table 2 also reports the ultimate shear strength, obtained by dividing $F_{v,u}$ by the cross-sectional area of the stud, and the ratio between the ultimate shear strength and the mean ultimate tensile strength obtained from the stud tensile coupon tests. It can be seen that while for the carbon steel studs this ratio is around 0.70, for the austenitic stainless steel studs this is around 0.80.

2.4. Stud weld characterisation and testing

2.4.1. Test setup and measurement

Tensile tests on welded studs were carried out to investigate any deterioration of mechanical properties arising from the welding process. The welding process used was arc stud welding, in accordance with ISO 14555:2017 [21] specifications for quality requirements, welding procedure specification, qualification testing of operators and testing of production welds. Carbon steel SD1 and austenitic EN 1.4301 stainless steel SD3 studs were arc stud-welded to lean duplex EN 1.4162 plates of the same thickness as those used for the flanges of the I-section beams

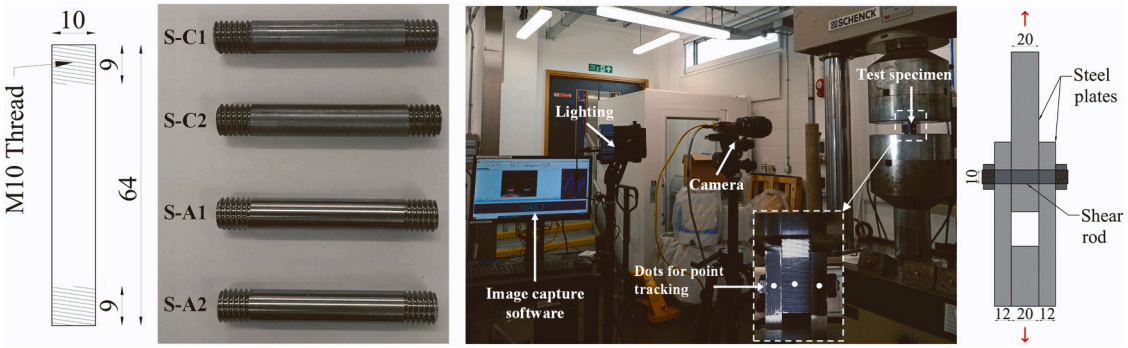

Fig. 5. (a) Dimensions of shear specimens in mm; (b) Double shear test setup.

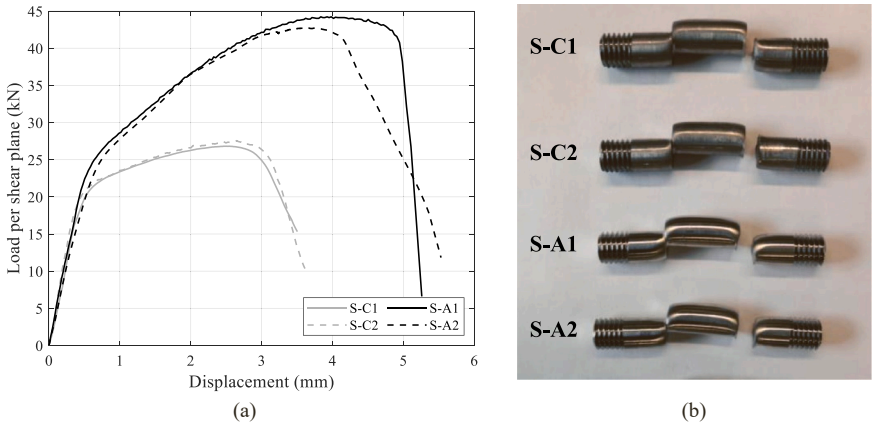

Fig. 6. (a) Load-slip results of double shear tests; (b) Photograph of fractured specimens.

Table 2
Summary of key results of double shear tests on studs.

Material	Specimen	k (N/mm)	$F_{v,u}$ (kN)	d_u (mm)	d_f (mm)	$f_{v,u}$ (MPa)	$f_{u,v}/f_u$ (-)
Carbon steel	S-C1	90,529	53.6	2.5	3.5	341	0.68
	S-C2	104,543	55.1	2.7	3.6	351	0.70
Austenitic EN 1.4301	S-A1	94,336	88.4	3.8	5.3	563	0.81
	S-A2	81,940	85.5	3.6	5.5	544	0.79

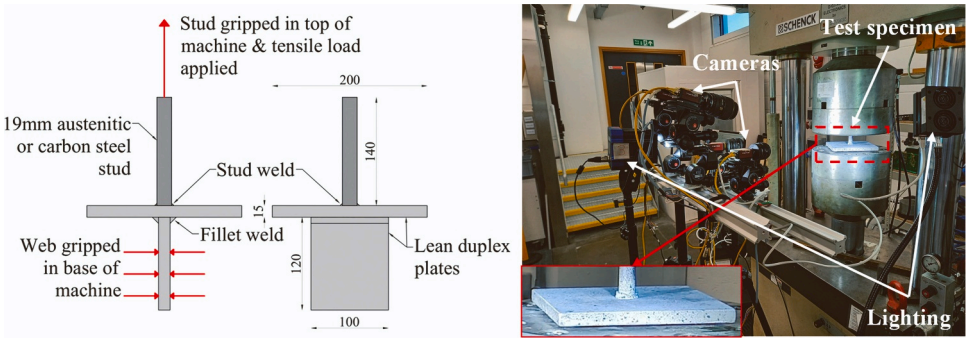

Fig. 7. (a) Diagram of welded stud specimens including dimensions in mm and loading; (b) Welded specimen test setup and measurement arrangement.

used in the push-out specimens, and the stud heads were removed to enable gripping in the test machine, as shown in Fig. 7**(a)**.

A total of five carbon steel specimens (W-C1 to W-C5) and five austenitic EN 1.4301 stainless steel specimens (W-A1 to W-A5) were tested. The tests were carried out in a Schenck 630 kN servo-hydraulic testing machine using the same strain rates as the tensile coupon tests i.e. at 0.007 % strain/sec up to 2 % strain and then at 0.025 % strain/sec until failure. DIC was used to capture the deformations of the welded specimens. The optimal camera arrangement was chosen through trial and error. Initially, two stereo camera pairs were setup, one in front of the test specimen and the other behind. This allowed out-of-plane deformations (i.e. bending due to stud misalignment) to be captured. However, since out-of-plane displacements were found to be negligible, a different arrangement of the cameras was chosen to capture the weld behaviour more closely. With this setup, one stereo pair parallel to the test specimen captured the height of the stud, and a second stereo pair was angled to point at the weld and the plate. The test setup and camera arrangement are shown in Fig. 7**(b)**. MatchID software was used to process the DIC images. The subset size ranged from 29 to 31 pixels and the step size was between 9–12 pixels for each specimen. A quadratic shape function was used with zero normalised sum of square differences (ZNSSD) correlation function and local bicubic spline interpolation function. Quadratic stereo transformation and Gaussian prefiltering were used, and for the automatic strain calculation the strain window was 15 pixels with Q8 interpolation and logarithmic Euler-Almansi strain tensor. For the purpose of the stress-strain curves, strains were calculated from the displacements recorded through DIC, using the MatchID virtual extensometer tool. The initial gauge length of the specimen was taken as the distance between the base of the weld and the top grips of the machine. The stresses in the stud were calculated from the recorded machine load divided by the stud cross-sectional area.

2.4.2. Results and discussion

The results of the welded stud tests are presented in Fig. 8 and Fig. 9 for the carbon steel and the austenitic stainless steel specimens, respectively. The key properties obtained from all tests are summarised in Table 3, where E is the Young's Modulus; $f_{0.2}$ is the 0.2 % proof stress; f_u is the ultimate tensile stress; ε_u is the strain at ultimate tensile stress and ε_f is the fracture strain. Two types of failure modes were observed, which were (i) stud necking failure and (ii) stud weld failure, as listed in Table 3 for each specimen. For the welded specimens which failed by stud necking, the mean values of the key properties agree with the stud coupon test results (Table 4), which are also depicted in Fig. 8 and Fig. 9 for comparison purposes. This shows that in these cases, there are no notable effects from the stud welding process. The lower E of the welded specimens may be because they were based on the DIC recorded data.

Fig. 10 provides a summary of the failure modes, the DIC longitudinal strain plots and the weld scans of each of the weld test specimens. One carbon steel specimen (W-C1) and three stainless steel specimens (W-A1, W-A4 and W-A5) exhibited stud weld failure. The carbon steel specimen W-C1 failed very abruptly at less than 1 % strain. While some small uniform deformation did occur in the shank of the stud, a clear strain concentration of up to 2 % can be seen at the stud-weld interface. Despite the austenitic stainless steel specimen W-A1 failing in the weld, it exhibited a ductile behaviour, with the stud reaching nearly 20 % strain before failing. Similarly, the austenitic stainless steel specimen W-A5 exhibited around 35 % strain before failing in the weld. The DIC results for W-A1 and W-A5 confirmed that significant uniform deformation took place in the shank of the studs, while the largest strains occurred around the weld, and the specimens reached close to the ultimate tensile strength of the stud before fracturing at the weld. Conversely, the W-A4 specimen fractured at less than 5 % strain and did not reach the ultimate tensile stress. The DIC results show that, for this specimen, little to no deformation occurred in the stud shank, and in the welded region the maximum longitudinal strain before fracture was only 15 %, which is significantly less than the 45 % and 75 % strains reached in specimens W-A1 and W-A5, respectively. The results indicate that W-C1 and W-A4 were weak specimens, with possible weld defects causing premature fracture.

The carbon steel specimens W-C2, W-C3 and W-C4 failed by stud necking, with large strain concentration in the necking region, as can be seen from the DIC results, and a relatively small stress concentration at the stud-weld interface. The W-C5 specimen failed at the machine grips due to an overly high gripping pressure and would have otherwise failed by necking in the stud shank rather than in the weld. The austenitic stainless steel specimens W-A2 and W-A3 also failed in the stud shank. No DIC is available for the W-A2 specimen, and due to paint cracking on the W-A3 specimen, the critical part of the necking region could not be correlated by DIC. However, the DIC results show similar pattern to other specimens, with higher strains in the shank of the stud and some strain concentration at the stud-weld interface, but less clear than in other specimens. Therefore, while a larger number of austenitic stainless steel specimens fractured in the weld, all austenitic stainless steel specimens experienced high deformations and four out of five specimens reached their ultimate capacity before failure.

To further analyse the stud welds, the specimens were cut down and x-ray computerised tomography (CT) scanning was used to observe the cross-section of the welds. The carbon steel specimens W-C1, W-C2, W-

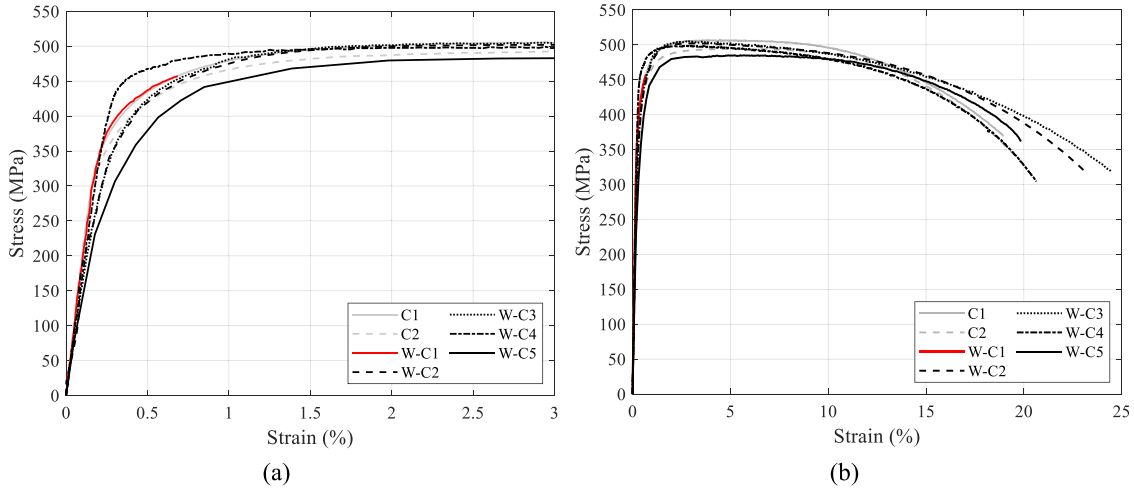

Fig. 8. Stress-strain response of carbon steel welded specimens compared to respective stud coupon tests; (a) small strain range; (b) full strain range. Red lines indicate tests where weld fracture occurred.

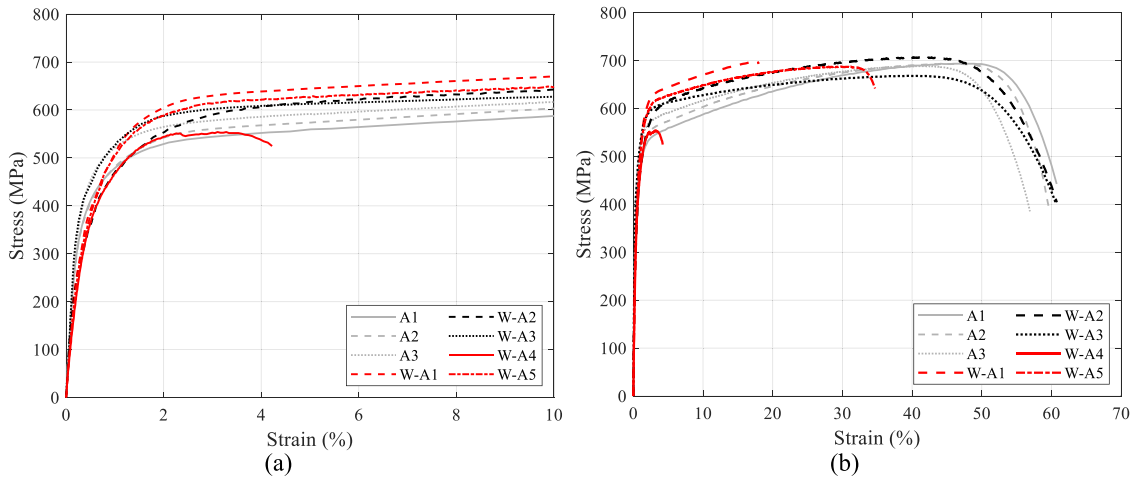

Fig. 9. Stress-strain response of austenitic stainless steel welded specimens compared to respective stud coupon tests; (a) small strain range; (b) full strain range. Red lines indicate tests where weld fracture occurred.

Table 3
Summary of key results from welded specimen tests. (*Not included in mean calculation).

Material	Specimen	E (MPa)	$f_{0.2}$ (MPa)	f_u (MPa)	ε_u (%)	ε_f (%)	Failure mode
Carbon steel	W-C1	205,000	422	457*	0.7*	0.7*	Weld
	W-C2	190,000	396	502	3.1	23.2	Stud necking
	W-C3	190,000	462	499	2.9	20.6	Stud necking
	W-C4	190,000	402	505	2.9	24.4	Stud necking
	W-C5	180,000	345	485	5.5	19.8	Stud necking
	Mean	191,000	405	498	3.6	22	
Austenitic EN 1.4301	W-A1	195,000	354	699*	17.6*	18.0*	Weld
	W-A2	185,000	325	707	41.0	60.8	Stud necking
	W-A3	190,000	432	668	39.3	60.9	Stud necking
	W-A4	150,000	340	554*	3.3*	4.2*	Weld
	W-A5	170,000	342	688*	28.1*	34.7*	Weld
	Mean	178,000	359	643	40.2	60.9	

Table 4
Comparison of mean results from tensile coupon and welded stud tests.

Material	Specimen	E (MPa)	$f_{0.2}$ (MPa)	f_u (MPa)	ε_u (%)	ε_f (%)
Carbon steel	Coupon	207,500	408	500	5.6	19.5
	Welded	191,000	405	490	3.6	22.0
Austenitic EN 1.4301	Coupon	193,000	398	692	44.8	58.5
	Welded	178,000	359	663	40.2	60.9

C3, W-A1, W-A2 and W-A3 were tested before scanning, while the austenitic stainless steel specimens W-C4, W-C5, W-A4 and W-A5 were scanned prior to testing. The W-C1 and W-A1 specimens could not be scanned since they failed in the weld. The CT scan images at the stud-plate interface are shown in Fig. 10. For the carbon steel specimens, the CT scans revealed a series of voids at the stud-plate weld interfaces. The microstructure of the weld of a representative austenitic EN 1.4301 stainless steel and carbon steel welded stud specimens was examined by etching at the Outokumpu R&D laboratory in Sweden. The austenitic stainless steel stud weld contained a mixture of austenite and duplex in the weldment, with 20–50 % ferrite content, and exhibited small pores. Conversely, excessive martensite was detected in the carbon steel stud weld and the heat affected zone (HAZ), and a large number of voids and pores were observed. The martensitic structure is stronger than the carbon steel stud material, but it is also brittle. This is believed to be the reason for the majority of the carbon steel specimens failing at the shank despite the large number of pores and voids observed, and for the brittle behaviour of the carbon steel specimen which failed at the weld.

3. Push-out tests

3.1. Eurocode 4 push-out test method

Standard push-out tests are described in Annex B of Eurocode 4 [15] for determining the resistance and slip capacity of shear connectors in composite beams. In the Second Generation of Eurocode 4 [22], Annex B will also give guidance for calculating the slip at which the resistance is first reached. This addition is to acknowledge that the ductility of shear connectors does not only depend on their slip capacity, and that an early attainment of the ultimate resistance and a large plateau in their load-slip behaviour are essential characteristics to ensure that the longitudinal shear force is redistributed between the studs along the beam.

The standard push-out specimen consists of two reinforced concrete slabs cast either side of a steel beam, with shear connectors welded to the flanges, as shown in Fig. 11. According to the standard testing procedure, the load is applied to the top of the steel beam up to 40 % of the expected failure load, then it is cycled 25 times between 5 % and 40 % of the expected failure load, to break any bond between the surface of the flange and slab, and then it is increased progressively until failure. The relative longitudinal slip between the steel beam and concrete slabs, as well as the transverse separation between the beam and each slab are measured continuously during the test, until at least the load drops to 20 % below the maximum load. The measured load-slip response, shown schematically in Fig. 12, is used to determine a number of response characteristics such as the characteristic resistance P_{Rk}, the shear connector stiffness k_{sc}, the slip capacity δ_u, and the elastic slip δ_{ke}. The definitions of these parameters are as follows: the characteristic

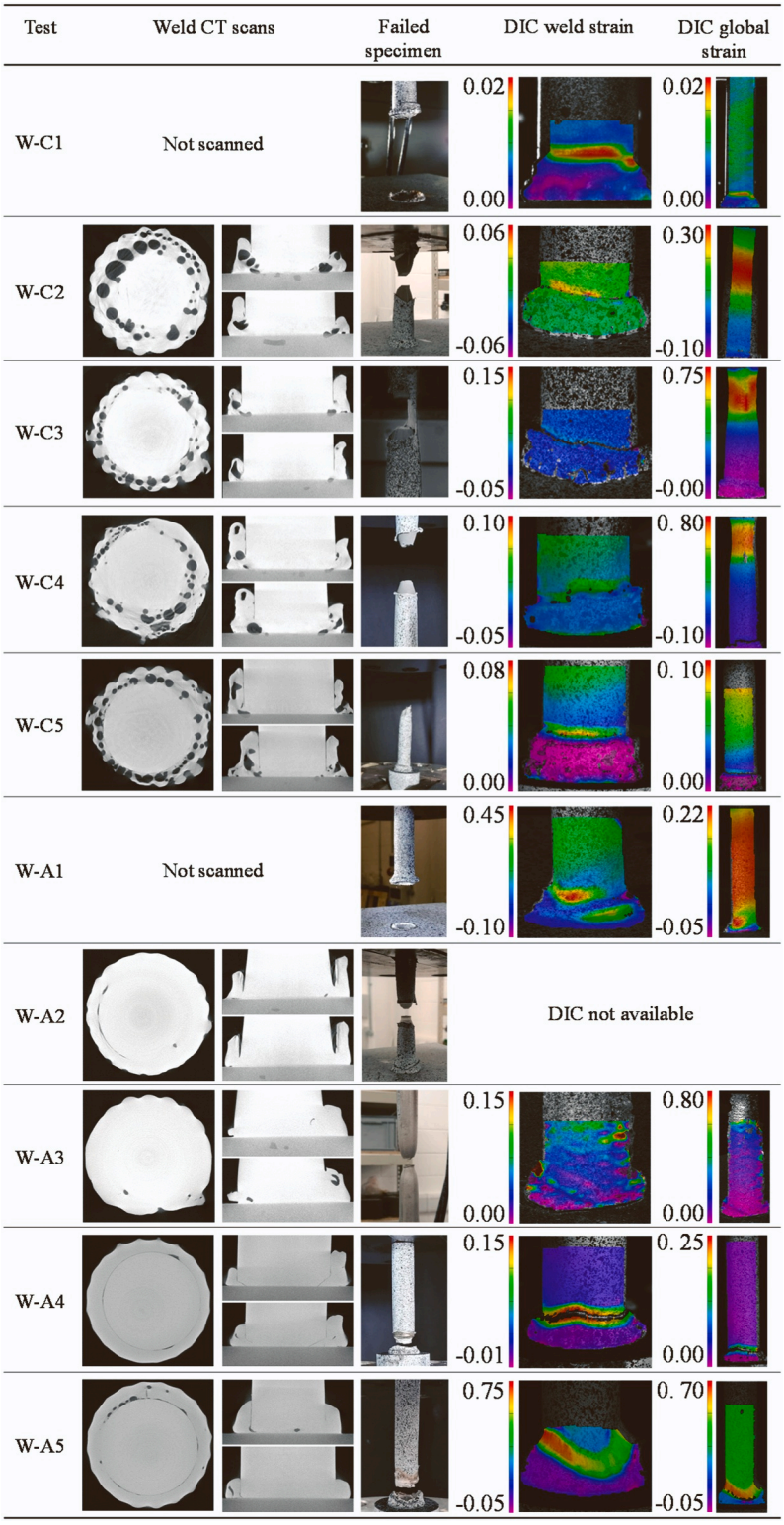

Fig. 10. Weld scans, specimen failure and DIC longitudinal strain plots.

resistance P_{Rk} is the measured total failure load, divided by the number of shear connectors, reduced by 10 %; the slip capacity δ_u is the slip measured on the descending part of the response at the characteristic resistance P_{Rk}; the shear connector stiffness k_{sc} is the secant stiffness at a load of $0.7P_{Rk}$ and corresponding slip s; and δ_{ke} is the elastic slip corresponding to when P_{Rk} is first reached. The elastic slip δ_{ke} is calculated based on the shear connector stiffness k_{se} i.e. $\delta_{ke} = P_{Rk}/(\tan\ k_{sc})$. Eurocode 4 [12] specifies that in order for a shear connector to be considered ductile, its characteristic slip capacity δ_{uk} should be at least 6 mm, with δ_{uk} defined as 0.9 of the slip capacity δ_u (i.e., $0.9\delta_u \geq 6$ mm for ductile connectors). In addition to this, the Second Generation of Eurocode 4 [22] will also require that a ductile shear connector should have an elastic slip δ_{ke} of less than 2.5 mm.

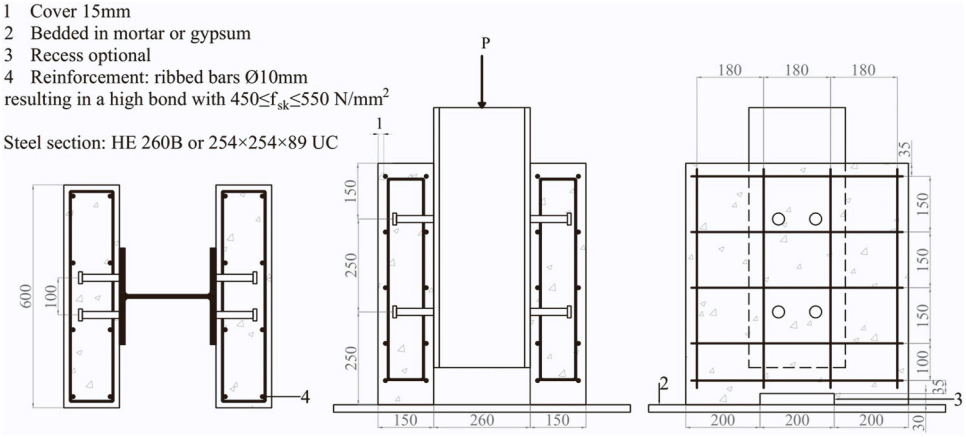

Fig. 11. Standard push-out test setup according to Eurocode 4 (dimensions in mm) [15].

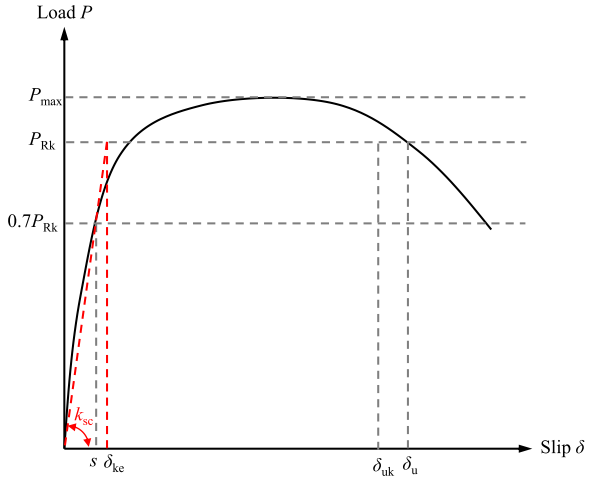

Fig. 12. Schematic representation of the load-slip response and definition of key characteristic parameters.

3.2. Preparation of test specimens

Due to the high ultimate strength of the austenitic stainless steel studs, the number of studs in each push-out specimen was halved so that the ultimate load could be achieved by the test rig. Two studs were welded to the centre of the flange on each side of the beam, at a spacing of 250 mm, giving a total of four studs per specimen. All studs were 19 mm diameter and had a total height of 150 mm. The studs were either carbon steel SD1 or austenitic EN 1.4301 stainless steel SD3. The beams were all lean duplex EN 1.4162 stainless steel. In order to be able to cast the slabs simultaneously in the horizontal position, the beams were comprised of two T-sections, which were bolted together after casting using two 10 mm thick S275 carbon steel plates and 20 M20 grade 8.8 zinc-plated bolts. Each T-section had a height of 130 mm, flange width of 130 mm, flange thickness of 15 mm and web thickness of 10 mm. The dimensions of the push-out test specimens are shown in Fig. 13.

Since the purpose of the tests was to observe the complete load-slip response of the shear studs, the desired failure mode was stud failure rather than early concrete failure, which would prevent the studs from reaching their full capacity. For the stainless steel studs with ultimate tensile strength $f_u = 692$ MPa, the predicted stud shear resistance from Eurocode 4 [15] is $P_{Rk,s} = 157$ kN (taking $\gamma_v = 1.00$) which gives an estimated total resistance of 628 kN for all four studs in the test arrangement. Hence, according to Eurocode 4 in order to have stud failure, the minimum concrete cylinder strength has to be $f_{ck} = 70$ MPa, which gives a concrete crushing resistance $P_{Rk,c} = 636$ kN. However, it should be noted that the Eurocode 4 [15] predictive equation for the stud shear resistance contains a factor of 0.8, which was largely based on reliability analyses to provide a safe prediction of design resistance and also to allow the use of the partial factor $\gamma_v = 1.25$ which is consistent with $\gamma_{M2} = 1.25$, i.e., the partial safety factor used for calculating the resistance of bolts. If the 0.8 factor is conservatively ignored, $P_{Rk,s} = 196$ kN per stud and 785 kN for the four studs. This requires a minimum concrete cylinder strength f_{ck} of 100 MPa. This concrete strength was therefore used as the basis for the carbon steel and stainless steel stud push-out tests. In addition, two specimens with f_{ck} of 50 MPa were also cast for the stainless steel stud specimens to investigate the effect of lower concrete strength on the measured response. Table 5 provides a summary of the stud material and concrete strength of the push-out test specimens. Three repeat tests were carried out for the carbon steel and stainless steel specimens with C100 concrete (i.e. specimens P-C1 to P-C3 and P-A1 to P-A3, respectively), while two repeat tests were performed for the stainless steel specimens with C50 concrete (i.e. specimens P-A4 and P-A5).

To achieve the C100 concrete strength, high strength class 52.5 N cement was used. In addition, superplasticiser was added to reduce the water to cement ratio whilst maintaining good workability, and microsilica was added in the form of SikaFume slurry admixture to assist with high strength gain. The adopted mix ratios per kg of cement were as follows: SikaFume microsilica slurry, 0.175 kg; sharp sand, 1.02 kg; 0–6 mm crushed granite, 1.53 kg; superplasticiser, 8.5 ml; and water, 0.17 kg. For the C50 concrete, Blue Circle High Strength Concrete 40 N ready-mix bags were used, with 2 l of water per 20 kg bag. The concrete slabs were cast in formworks assembled using 12 mm thick plywood and aluminium brackets. The insides of the formwork were greased with a mould release oil. The surface of the beam flange was also greased to prevent bonding with the concrete, so that the shear resistance obtained from the push-out tests was provided solely by the studs. Ribbed reinforcement bars of 10 mm diameter were placed inside the formwork, with 15 mm spacers on each side to ensure cover. The concrete was poured into the formwork in 3 layers After each layer, a vibrating poker was used to compact the concrete and evenly fill the spaces between the reinforcing bars. The top of the concrete was smoothed using a float and covered with damp hessian. The slabs were left in the formwork for 48 h, and once the formwork was removed, the slabs were again covered with damp hessian and tarpaulin to maintain a moist curing environment. A total of 5 concrete cubes of 100 mm in size were cast and cured alongside each slab, 2 of which were tested at 28 days and the remaining 3 cubes were tested on the same day the push-out specimen was tested. The measured mean cube strengths at 28 day $f_{cube,28}$ and test day $f_{cube,test}$ for each of the specimens are reported in Table 6. The equivalent cylinder compressive strength f_{ck} was calculated using Eq. (1) which was proposed by L'Hermite [23], where $f_{cube,100}$ is the

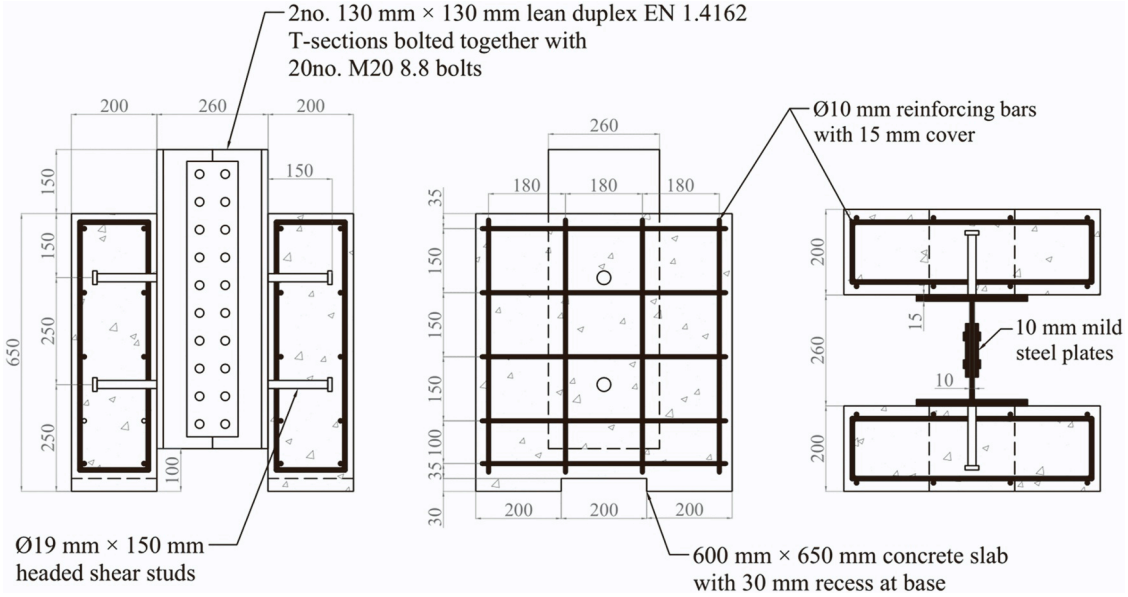

Fig. 13. Dimensions of push-out test specimens (mm).

Table 5
Materials of push-out test specimens.

Specimen	Stud material	Concrete strength
P-C1	Carbon steel	C100
P-C2	Carbon steel	C100
P-C3	Carbon steel	C100
P-A1	Austenitic EN 1.4301	C100
P-A2	Austenitic EN 1.4301	C100
P-A3	Austenitic EN 1.4301	C100
P-A4	Austenitic EN 1.4301	C50
P-A5	Austenitic EN 1.4301	C50

mean 100 mm cube compressive strength.

$$f_{ck} = \left[0.76 + 0.2\log_{10}\left(\frac{0.96f_{cube,100}}{19.6}\right)\right] \times 0.96f_{cube,100} \quad (1)$$

3.3. Push-out test setup and procedure

Fig. 14**(a)** shows the overall setup of the push-out tests. A 1000 kN capacity Instron 8805 hydraulic actuator was used to apply the load. The base of the slab was fixed onto the test bed using dental plaster. A series of LED optical trackers were attached to the beam and slabs to measure the longitudinal slip and transverse separation of the beam from the slabs, the locations of which are as shown in Fig. 14**(b)**. A camera system was used to track the positions of the LEDs in the *x*-, *y*- and *z*-directions throughout the test. A rubber sheet was placed on top of the beam to distribute the load from the actuator evenly, and aluminium shims were added if required, to level the surface between the two beam halves. As per the method in Annex B of Eurocode 4 [15], the first test in each group was run as a static test under displacement control at a rate of 0.3 mm/min, to identify the peak load. Subsequent tests were run with 25 initial cycles between 5 % and 40 % of the maximum load, at a rate of 200 kN/min; after that, the test was switched to displacement control at a rate of 0.3 mm/min. The tests were continued until the load dropped by at least 20 % below the peak load.

Table 6
28-day and test day concrete strengths for push-out specimens.

Specimen	$f_{cube,28}$ (MPa)	$f_{cube,test}$ (MPa)	$f_{ck,28}$ (MPa)	$f_{ck,test}$ (MPa)
P-C1	107	119	93	104
P-C2	102	99	88	85
P-C3	116	112	101	97
Mean	108	110	94	96
P-A1	120	120	105	105
P-A2	100	107	86	93
P-A3	115	113	100	98
Mean	111	113	97	99
P-A4	60	60	49	49
P-A5	58	59	47	48
Mean	69	60	48	49

3.4. Results and discussion

The measured load-slip responses of the push-out tests are shown in Fig. 15. The key response characteristics including the maximum load per shear connector P_u, characteristic resistance P_{Rk}, shear connector stiffness k_{sc}, elastic slip δ_{ke}, slip capacity δ_u and characteristic slip capacity δ_{uk} ($= 0.9\delta_u$) are presented in Table 7. All the push-out specimens failed at the stud with little concrete damage. The results show that the austenitic stainless steel studs have greater load capacity than the carbon steel studs. The average P_u for the austenitic stainless steel studs in C100 concrete is 32 % higher than for the carbon steel studs. The austenitic stainless steel studs also show significantly greater ductility than the carbon steel studs, with the average δ_u for the austenitic stainless steel studs in C100 concrete being 262 % larger than for the carbon steel studs. All the austenitic stainless steel studs showed a characteristic slip capacity δ_{uk} well over the 6 mm required in Eurocode 4 for ductile studs, and were able to attain their characteristic resistance at an elastic slip of less than 2.5 mm. Conversely, the carbon steel studs were not able to meet the 6 mm slip requirement. Also, one of the push-out specimens with carbon steel studs (specimen P-C1) showed an unexpected drop in resistance shortly after the peak load was reached, after which the resistance was maintained for around 1.5 mm and then gradually decreased until the test was stopped (see Fig. 15**(a)**). This drop in resistance is attributed to the premature failure of one of the studs. For this reason, the slip capacity δ_u was not evaluated for specimen P-C1. The push-out specimens with carbon steel studs also showed significant variability in the slip behaviour. These two features observed from the push-out tests with carbon steel studs can be explained by the irregularities and imperfections that occurred when the studs were welded to the lean duplex stainless steel beams, as revealed by the CT scan images shown in Fig. 10. It is therefore concluded that carbon steel shear studs

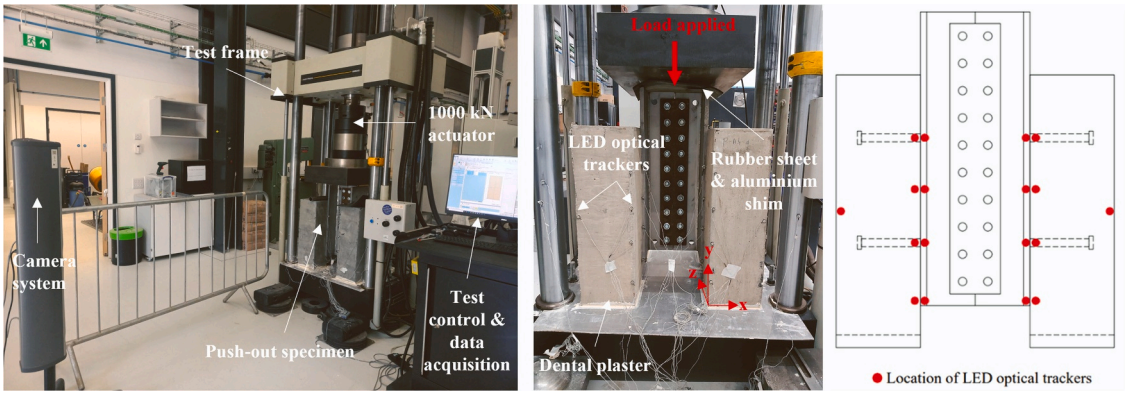

(a) (b)

Fig. 14. (a) Push-out test setup; (b) Location of LED optical trackers.

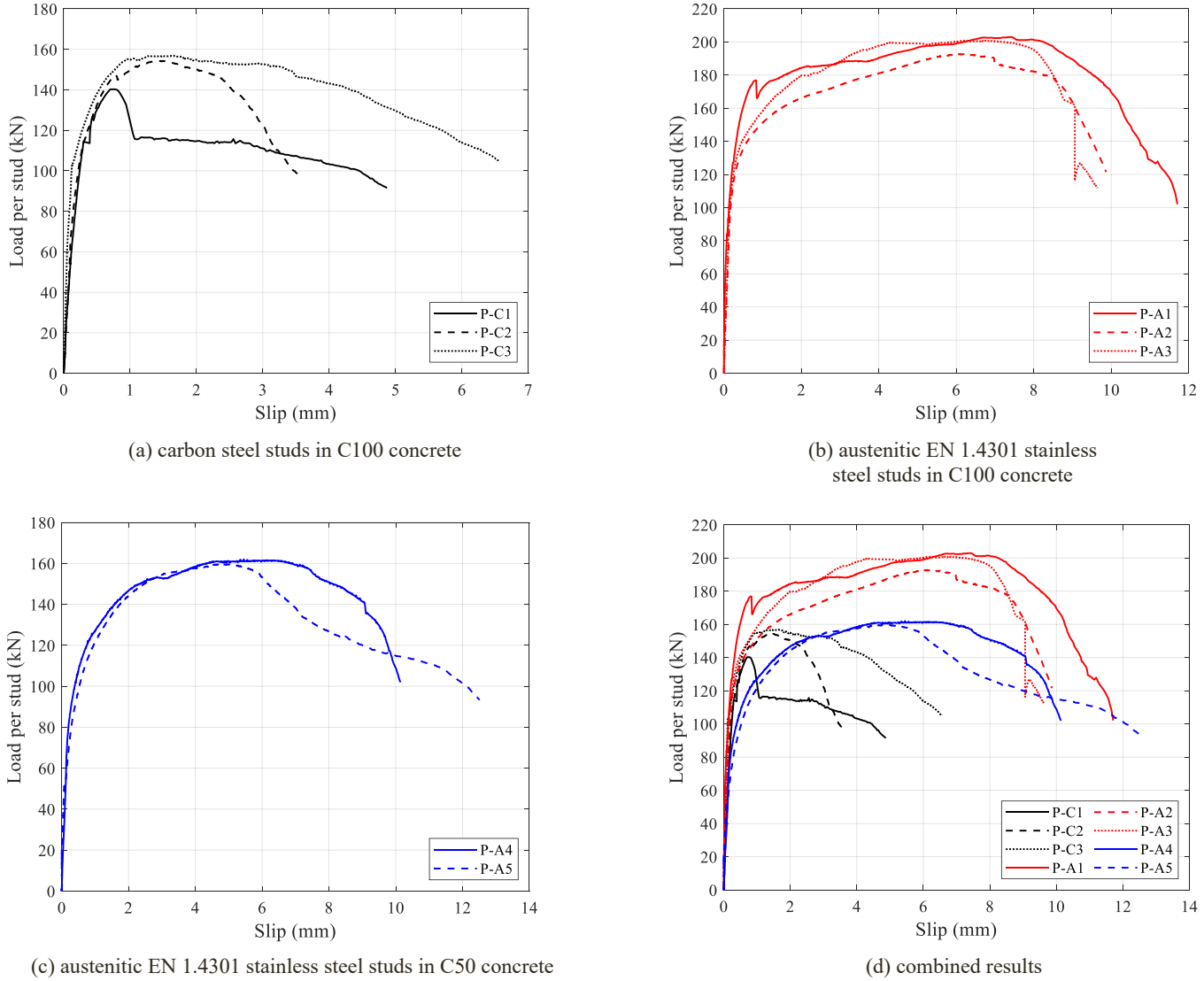

(a) carbon steel studs in C100 concrete

(b) austenitic EN 1.4301 stainless steel studs in C100 concrete

(c) austenitic EN 1.4301 stainless steel studs in C50 concrete

(d) combined results

Fig. 15. Load-slip response of push-out tests on (a) carbon steel studs in C100 concrete; (b) austenitic EN 1.4301 stainless steel studs in C100 concrete; (c) austenitic EN 1.4301 stainless steel studs in C50 concrete; (d) combined results.

welded to lean duplex stainless steel beams cannot be considered to provide ductile behaviour in accordance with the requirements of Eurocode 4, and their use is not recommended due to their poor weld quality which leads to unreliable structural behaviour.

The austenitic stainless steel studs in C50 concrete had a 23 % lower capacity than those in C100 concrete. However, the resistance of these

Table 7
Results from push-out tests.

Stud material	Specimen	P_u (kN)	P_{Rk} (kN)	k_{sc} (kN/mm)	δ_{ke} (mm)	δ_u (mm)	δ_{uk} (mm)	Failure mode
Carbon steel	P-C1	141	127	444	0.30	-	-	Stud failure
	P-C2	154	139	416	0.33	2.6	2.3	Stud failure
	P-C3	157	141	549	0.26	4.2	3.8	Stud failure
	Mean	151	136	470	0.30	3.4	3.1	Stud failure
Austenitic EN 1.4301	P-A1	203	183	533	0.30	9.4	8.5	Stud failure
	P-A2	193	174	271	0.64	8.7	7.8	Stud failure
	P-A3	201	181	282	0.64	8.5	7.7	Stud failure
	Mean	199	179	362	0.53	8.9	8.0	Stud failure
	P-A4	162	146	255	0.57	8.6	7.7	Stud failure
	P-A5	160	144	201	0.71	6.7	6.0	Stud failure
	Mean	161	145	228	0.64	7.7	6.9	Stud failure

specimens was still governed by stud failure. The lower resistance of the austenitic stainless steel studs in C50 concrete was accompanied by a greater slip prior to the attainment of the characteristic resistance P_{Rk}, which led to bending in the studs. This suggests that the interaction of bending and shear stresses reduced the stud capacity. P-A3 showed a sudden drop in load at a slip of 9 mm; at this point, a crack was heard, which indicates one of the studs had fractured. Aside from this, most of the specimens remained intact after the load dropped below 80 % of the peak. After this point, the actuator was used to apply more displacement to the beam, forcing the studs to fracture so that the beam and slabs could be separated for visual inspection. Fig. 16 shows photographs of the damaged steel and concrete surfaces after the tests for one of each of the different test series: P-A1 (austenitic stainless steel stud, C100 concrete); P-C1 (carbon steel stud, C100 concrete); and P-A4 (austenitic stainless steel stud, C50 concrete). Since the studs were forcibly fractured after the tests, these images are not completely representative of the stud behaviour during the test. However, they provide a useful comparison of the relative damage between each series of tests. All of the studs fractured in or adjacent to the weld. The weld collars in one of the studs from specimens P-A1 and P-A4 remained attached to the flange. The voids in the weld of P-C1 were evident after the test, whereas the welds in the austenitic stainless steel specimens appeared more homogenous. Slightly more concrete crushing was observed in P-A1 than P-C1, with the visible damage extending 36 mm below the stud in P-A1 compared to 23–31 mm in P-C1. As expected, P-A4, with the weaker concrete, showed the most visible concrete damage, extending 38–55 mm below the stud. However, all of the visible concrete crushing was localised indicating the dominant failure mechanism was stud fracture.

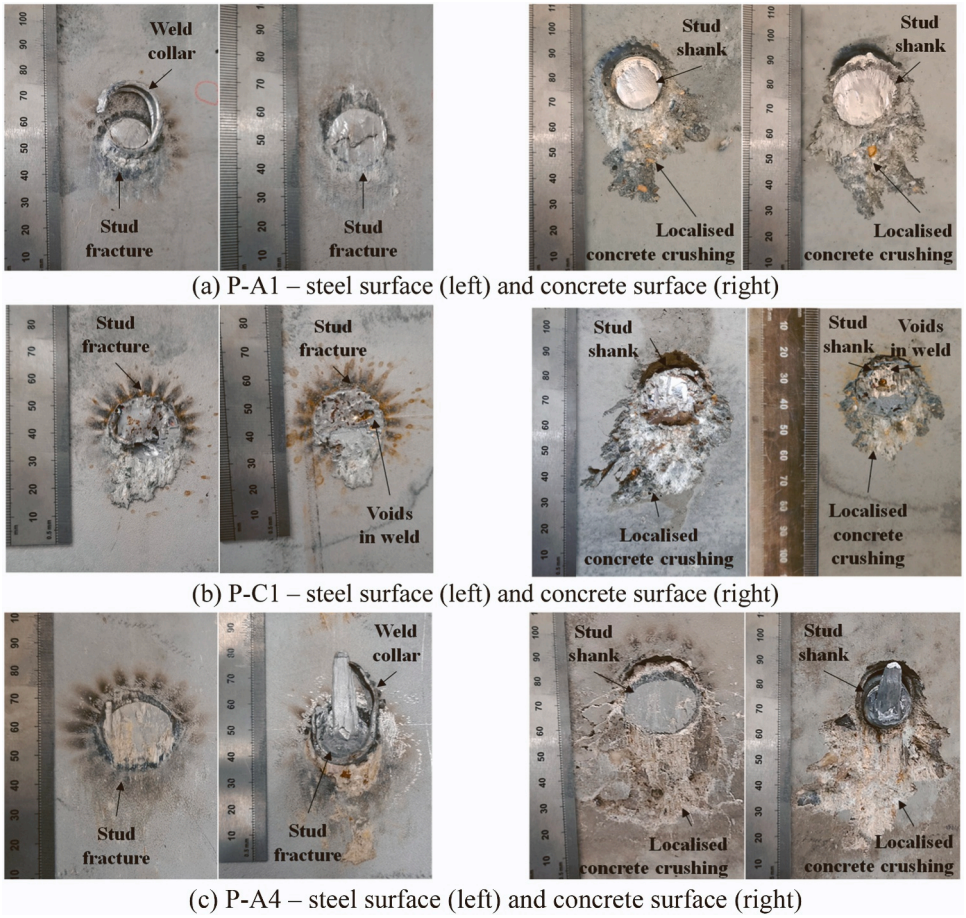

Fig. 16. Photographs of steel and concrete damage after push-out tests.

4. Comparison of push-out test results with code predictions

Design equations for calculating the shear resistance of headed studs in solid slabs are provided in Eurocode 4 [15], the American specifications AISC-360 [24] and the AASHTO Bridge Design Specification [17], the Japanese specification JSCE [25], the Australian and New Zealand standard AS/NZS-2327 [26] and the Canadian specification CSA-S16 [27]. The resistance equations in the current version (9th edition) of the AASHTO Bridge Design Specification (AASHTO 9) will be revised for the 10th edition (AASHTO 10). With the exception of AASHTO 10, in all the other design codes, two equations are provided for determining the resistance of the shear connectors, which refer to (i) failure of the stud (stud failure) and (ii) failure of the concrete surrounding the stud (concrete failure). The design resistance is then taken as the smaller value of these two predicted resistances. Table 8 presents a summary of the different codified design resistance equations, where the basic material and geometric variables used are defined as follows: d is the diameter of the stud shank; h is the overall height of the stud; f_u is the ultimate tensile strength of the stud material; f_{ck} is the compressive cylinder strength of the concrete; and E_c or E_{cm} is the secant modulus of elasticity of the concrete.

Table 8 also includes the limitations on the ultimate tensile strength and dimensions of the studs, which are associated with the resistance equations for stud failure, and the value for the resistance factor (i.e. γ or ϕ) used with each equation. The limitation on the stud ultimate tensile strength reflects the strength of the tested studs that were included in the reliability analysis used for the calibration of the resistance equations, and also the strength of the studs that are specified in the relevant product standard that is applicable to the design code. AASHTO 9, JSCE and CSA-S16 assume that the resistance to steel failure is given by the tensile resistance of the stud, which might be viewed as unusual considering that the stud fails in shear and not in tension. However, this may be justified by the larger diameter of the stud weld collar. Nonetheless, in AASHTO 10, the nominal resistance to steel failure will be reduced to 70 % of the nominal tensile resistance of the stud. Note that although the resistance factor will be increased from $\phi_{sc} = 0.85$ to 1.00, the design resistance to steel failure in AASHTO 10 will still be 82 % of that given in the AASHTO 9 equation. AASHTO 10 will also eliminate the equation that accounts for concrete failure. The removal of this equation is justified by the use of more stringent limits on the h/d ratio of the studs. Thus, for studs that meet the requirements in AASHTO 10, checking only the resistance to stud failure will be considered to be sufficient when designing the shear connector, even when the governing failure mode is concrete failure.

As Table 8 shows, Eurocode 4, AASHTO, JSCE, AS/NZS-2327 and CSA-S16 give resistance factors, γ or ϕ, for calculating the design resistance of the shear connector (i.e. $P_{Rd} = P_{Rk}/\gamma$ or $P_{Rd} = \phi P_{Rk}$, where P_{Rk} is the characteristic resistance), whereas AISC-360 does not give any resistance factor. This is because while in most design codes the design resistance of the stud shear connector is compared to the horizontal shear force that results at the interface between the concrete slab and the steel section when the design value of the composite beam bending resistance is reached, in AISC-360 this comparison is based on the nominal values of the shear connector resistance P_n and the nominal value of the shear force. This may be interpreted as if the resistance factor associated with the resistance equations for stud shear connectors given in AISC-360 is the same as the resistance factor used for calculating the design bending resistance of the composite beam, which is $\phi = 0.9$. In AASHTO, the design resistance of the shear connector is compared to the nominal value of the shear force. However, because in AASHTO the resistance factor for the bending resistance of the composite beam is equal to 1.0, the nominal value of the shear force coincides with its design value.

Fig. 17 presents a graphical comparison of the above-mentioned design codes, where the predicted unfactored stud resistance P_{Rk} or P_n is plotted against different concrete strengths f_{ck}. At low concrete strengths, the stud resistance is controlled by the crushing of the concrete surrounding the stud shank, while at high concrete strengths, the stud resistance is determined by the failure of the stud. The comparisons are shown for two values of the stud ultimate strength ($f_u = 500$ MPa and 692 MPa), corresponding to the average values of the carbon steel and stainless steel studs tested herein, and a stud diameter of 19 mm. The

Table 8
Summary of design resistance equations for headed shear studs in solid slabs according to international design codes.

Design code	Stud failure	Concrete failure	Limitation on stud	Resistance factor
EC4	$P_{Rd,s} = \frac{0.8 f_u \pi d^2/4}{\gamma_v}$	$P_{Rd,c} = \frac{0.29 \alpha d^2 \sqrt{f_{ck} E_{cm}}}{\gamma_v}$	$f_u \le 500$ MPa 16 mm $\le d \le$ 25 mm For $3 \le h/d \le 4$, $\alpha = 0.2(h/d+1)$ For $h/d > 4$, $\alpha = 1$	$\gamma_v = 1.25$
AISC−360	$P_{n,s} = 0.75 f_u \pi d^2/4$	$P_{n,c} = 0.5 \frac{\pi d^2}{4} \sqrt{f_{ck} E_c}$	$f_u = 450$ MPa $d \le 25$ mm $h/d \ge 4$	-
AASHTO 9	$P_{Rd,s} = \phi_{sc} f_u \pi d^2/4$	$P_{Rd,c} = \phi_{sc} 0.5 \frac{\pi d^2}{4} \sqrt{f_{ck} E_c}$	$f_u = 415$ MPa $h/d \ge 4$	$\phi_{sc} = 0.85$
AASHTO 10	$P_{Rd,s} = \phi_{sc} 0.70 f_u \pi d^2/4$	-	$f_u = 415$ MPa $h/d \ge 5$ for normal-weight concrete $h/d \ge 7$ for light-weight concrete	$\phi_{sc} = 1.00$
JSCE	$P_{Rd,s} = \frac{f_u \pi d^2/4}{\gamma_b}$	$P_{Rd,c} = \frac{31 \pi d^2/4 \sqrt{(h/d) f_{ck}} + 10000}{\gamma_b}$	402 MPa $\le f_u \le$ 549 MPa 13 mm $\le d \le$ 31 mm 50 mm $\le h \le$ 210 mm	$\gamma_b = 1.3$
AS/NZS−2327	$P_{Rd,s} = \phi 0.7 d^2 f_u$	$P_{Rd,c} = \phi 0.29 d^2 \sqrt{f_{ck} E_c}$	$f_u \le 500$ MPa 16 mm $\le d \le$ 25 mm $h/d \ge 4$	$\phi = 0.80$
CSA-S16	$P_{Rd,s} = \phi_{sc} f_u \pi d^2/4$	$P_{Rd,c} = \phi_{sc} 0.5 \pi d^2/4 \sqrt{f_{ck} E_c}$	f_u typically taken as 450 MPa $h/d \ge 4$	$\phi_{sc} = 0.80$

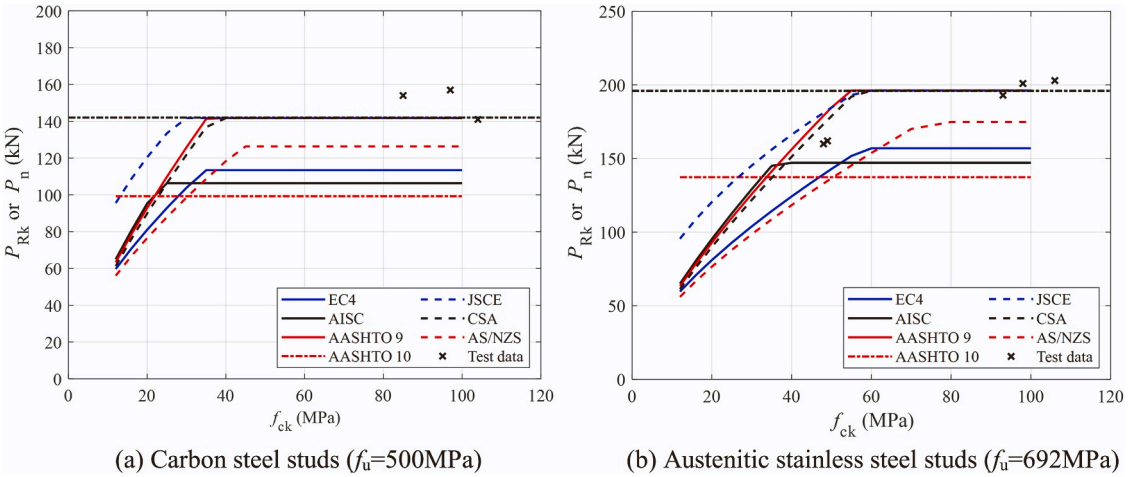

Fig. 17. Unfactored stud resistance as a function of concrete strength according to different international design codes and stud resistance from push-out tests.

Table 9
Comparison of test results with unfactored resistance predicted from international design codes (S=stud failure, C=concrete failure).

Stud	Test	d (mm)	h (mm)	f_u (MPa)	f_{ck} (MPa)	$P_{u,test}$ (kN)	$P_{u,test}/P_{Rk}$ or P_{nom}						
							EC4	AISC-360	AASHTO 9	AASHTO 10	JSCE	AS/NZS- 2327	CSA-S16
Carbon steel	P-C1	19	150	500	104	141 [s]	1.24 [s]	1.33 [s]	0.99 [s]	1.42 [s]	0.99 [s]	1.12 [s]	0.99 [s]
	P-C2	19	150	500	85	154 [s]	1.36 [s]	1.45 [s]	1.09 [s]	1.55 [s]	1.09 [s]	1.22 [s]	1.09 [s]
	P-C3	19	150	500	97	157 [s]	1.38 [s]	1.48 [s]	1.11 [s]	1.58 [s]	1.11 [s]	1.24 [s]	1.11 [s]
Austenitic EN 1.4301	P-A1	19	150	692	106	203 [s]	1.29 [s]	1.38 [s]	1.03 [s]	1.48 [s]	1.03 [s]	1.16 [s]	1.03 [s]
	P-A2	19	150	692	93	193 [s]	1.23 [s]	1.31 [s]	0.98 [s]	1.41 [s]	0.98 [s]	1.10 [s]	0.98 [s]
	P-A3	19	150	692	98	201 [s]	1.28 [s]	1.37 [s]	1.02 [s]	1.46 [s]	1.02 [s]	1.15 [s]	1.02 [s]
	P-A4	19	150	692	49	162 [s]	1.15[c]	1.10 [s]	0.89[c]	1.18 [s]	0.89[c]	1.20[c]	0.92[c]
	P-A5	19	150	692	48	160 [s]	1.15[c]	1.09 [s]	0.89[c]	1.16 [s]	0.88[c]	1.20[c]	0.92[c]

stud resistances obtained from the push-out tests are also included in the figure for comparison purposes. The resistances obtained from the push-out test are also compared in Table 9 to the unfactored resistances P_{Rk} or P_n (i.e., all resistance factors γ or ϕ set to unity) predicted by the international codes. For the carbon steel stud tests, all the code predictions correspond to the stud shear failure mode. The tests exhibit higher capacities than the predicted resistances of all the above codes, except for P-C1 which had a test-to-predicted resistance ratio = 0.99 from AASHTO 9, JSCE and CSA-S16. The most conservative resistance ratios are obtained for AASHTO 10, which has the lowest factor of 0.70 on the equation for stud failure and underpredicts the stud capacity by 42 % to 58 %. For the austenitic EN 1.4301 stainless steel stud tests in C100 concrete (P-A1 to P-A3), all code predictions correspond to stud shear failure mode. For these specimens, AASHTO 9, JSCE and CSA-S16 give the same and closest predictions since they all have the same unfactored steel failure equation, whereas more conservative resistances are predicted by Eurocode 4, AISC-360, AASHTO 10 and AS/NZS-2327 with the level of conservatism varying due to the different values of the coefficients (i.e., 0.8 for Eurocode 4, 0.75 for AISC-360, 0.70 for AASHTO 10 and $0.7/(\pi/4) = 0.89$ for AS/NZS-2327) used in the stud failure resistance equations. For the austenitic EN 1.4301 stainless steel stud tests in C50 concrete (i.e. P-A4 and P-A5), the predicted failure mode by all codes, except AISC-360 and AASHTO 10, is concrete failure, despite the test failure mode being controlled by stud failure. In this case, Eurocode 4, AISC 360, AASHTO 10 and AS/NZS 2327 predict safe-sided resistances, with those from AISC-360 being the closest to the test results, while AASHTO 9, JSCE and CSA-S16 overestimate the resistance by around 10 %. Overall, the stud resistance equations given in Eurocode 4 and AASHTO 10, provide safe-sided predictions for all tested studs.

Results of push-out tests on carbon steel studs, in which the ultimate capacity was governed by stud failure, were collected from the available literature [28–44] to assess how their structural performance compares with that of the studs investigated in this study, in particular the austenitic EN 1.4301 stainless steel studs. Fig. 18 plots the experimental stud resistances collected from the literature and this study against the unfactored predicted stud resistances from Eurocode 4 [15] and AASHTO 10, using the measured steel and concrete material properties. In Fig. 18, the resistance predicted by the design code corresponds to the resistance to stud failure. These stud resistance equations have been chosen for the comparison because these are the equations that are used when designing steel-concrete composite bridges in the U.S. and Europe. The figure shows that the resistance of the austenitic stainless steel and carbon steel studs obtained from the push-out tests in this study follow the same trend as that of the tests collected from the literature when compared to the codes' resistance, suggesting that the resistance equations developed for shear connectors made with carbon steel studs can also be applied to shear connectors made with austenitic EN 1.4301 stainless steel studs.

5. Conclusions

This paper presented an experimental study on the behaviour of austenitic EN 1.4301 stainless steel SD3 studs and carbon steel SD1 studs welded to lean duplex EN 1.4162 stainless steel beams. The key conclusions are as follows:

- The stud tensile coupon tests and double shear tests showed that the austenitic EN 1.4301 studs exhibit higher strength and ductility than the carbon steel studs. Tensile tests on welded studs (austenitic studs welded to lean duplex plates, and carbon steel studs welded to lean duplex plates) revealed that the welded region in the austenitic stainless steel studs exhibited a ductile behaviour compared with those of the carbon steel studs, where premature brittle failure was observed.

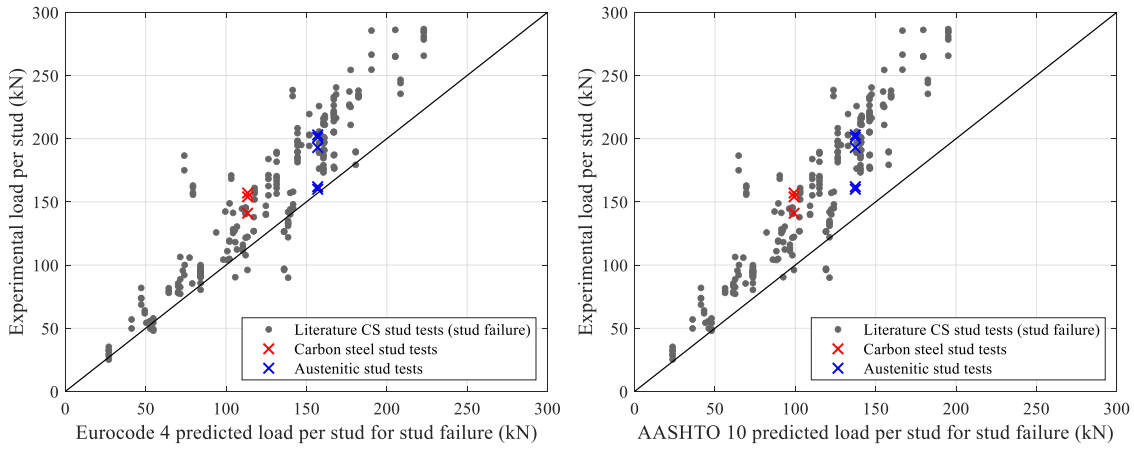

Fig. 18. Comparison of test results with Eurocode 4 and AASHTO 10 predicted stud resistance for carbon steel stud push-out tests reported in the literature and push-out tests from this study.

- X-ray computerised tomography (CT) scanning and etching conducted to inspect the weld region and correlate the microstructural changes to the material response showed a significant number of pores and voids in the welded region of the carbon steel studs, along with a high martensite content, which resulted in a brittle and unpredictable performance of the weld. In the austenitic stainless steel welded studs only small pores were visible in the welded region, with the weldment exhibiting a more ductile behaviour.
- Push-out tests on the carbon steel and the austenitic stainless steel studs welded to lean duplex beams were conducted to assess and compare the performance of the shear connectors embedded in a solid concrete slab. The austenitic stainless steel studs were found to achieve significantly larger capacity and ductility than the carbon steel studs, and were able to meet the Eurocode 4 ductility requirements for ductile shear connectors. The carbon steel studs, on the other hand, did not demonstrate enough ductility to satisfy the requirements of Eurocode 4 and one of the push-out specimens suffered a premature failure of one of the studs. This was attributed to the poor quality of the weld that was achieved when stud welding the carbon steel studs to the lean duplex stainless steel plates, which has led to conclude that carbon steel studs should not be used in composite beams made with lean duplex stainless steel sections.
- In spite of the resistance of all austenitic stainless steel studs being governed by stud failure (as opposed to concrete failure), the resistance of the studs in C50 concrete was found to be lower than that of the studs in C100 concrete, which is attributed to the interaction between bending and shear resulting from some localised crushing of the concrete around the stud. This interaction will be further investigated through finite element analysis, using numerical push-out tests models that have been validated using the test results presented in this paper.
- The shear resistances obtained from the push-out tests were also compared to the predicted resistance by several international design codes, and to the resistance from push-out tests on carbon steel studs collected from the literature (i.e. carbon steel studs welded to carbon steel beams). In particular, the stud resistance equations given in Eurocode 4 and AASHTO 10, which are the resistance equations that are used when designing the shear connectors of composite bridges, were found to provide safe-sided predictions, and the resistance performance of the austenitic stainless steel studs was found to be comparable to that of the carbon steel studs collected from the literature, suggesting that these resistance equations could potentially be applicable also to austenitic stainless steel studs welded to duplex stainless steel.

Declaration of Competing Interest

The authors declare that they have no known competing financial interests or personal relationships that could have appeared to influence the work reported in this paper.

Data availability

Data will be made available on request.

Acknowledgements

The authors would like to thank Outokumpu for the supply of test materials and undertaking the etching microscopic examination, and the National Facility for X-ray Computed Tomography at University of Southampton for allowing use of the CT scanners, funded by EPSRC grant no. EP/T02593X/1.

References

[1] E. Schedin and A. Backhouse, “Stainless steel composite bridge study - A summary of ARUP reports,” 2019.
[2] F. Meza and N. Baddoo, “Life Cycle Cost Assessment of a Stainless Steel Highway Bridge,” 2023, The Steel Construction Institute.
[3] P. Albrecht and A.H. Naeemi, “Performance of weathering steel in bridges. NCHRP Report 272.,” 1984.
[4] Team Stainless, “The Global Life Cycle of Stainless Steels,” 2023. Accessed: Feb. 16, 2024. [Online]. Available: ⟨https://www.worldstainless.org/about-stainless/environment/recycling/⟩.
Mameng SH, et al. Duplex stainless steels as a structural material for long life bridge construction. IABSE Symp Guimaraes 2019.
[6] S.H. Mameng and A. Backhouse, “Duplex Stainless Steels: Sustainable Materials for Highly Durable Structures,” in IABSE Congress New York, 2019.
[7] J.A. Sobrino, “The fort york footbridges in Toronto. The first duplex stainless steel bridges in North America,” in IABSE Congress New York, 2019.
[8] Johnson R.P., (2004). Composite Structures of Steel and Concrete. third ed. Blackwell Publishing.
[9] Arrayago I, Ferrer M, Marimon F, Real E, Mirambell E. Experimental investigation on ferritic stainless steel composite slabs. Eng Struct 2018;174:538–47. https://doi.org/10.1016/j.engstruct.2018.07.084.
[10] Cashell K, Baddoo N. Experimental assessment of ferritic stainless steel composite slabs. Composite Construction in Steel and Concrete VII. Reston, VA: American Society of Civil Engineers,; 2016. p. 300–13. https://doi.org/10.1061/9780784479735.023.
[11] Shamass R, Cashell K. Analysis of stainless steel-concrete composite beams. J Constr Steel Res 2019;152:132–42. https://doi.org/10.1016/j.jcsr.2018.05.032.
[12] Zhou Y, Uy B, Wang J, Li D, Li X. Behaviour and design of stainless steel shear connectors in composite beams. Steel Compos Struct 2023;46(2):175–93. https://doi.org/10.12989/scs.2023.46.2.175.
[13] Zhou Y, Uy B, Wang J, Li D, Huang Z, Liu X. Behaviour and design of stainless steel-concrete composite beams. J Constr Steel Res 2021;185:106863. https://doi.org/10.1016/j.jcsr.2021.106863.

[14] Gardner L, Kucukler M, Macorini L. Deformation-based design of composite beams. Composite Construction in Steel and Concrete VII. Reston, VA: American Society of Civil Engineers,; 2016. p. 131–45. https://doi.org/10.1061/9780784479735.011.
[15] EN 1994–1-1:2004 Eurocode 4. Design of composite steel and concrete structures. General rules and rules for buildings, CEN, 2004.
[16] EN 1994–2:2005 Eurocode 4. Design of composite steel and concrete structures. General rules and rules for bridges, CEN, 2005.
[17] AASHTO LRFD bridge design specifications, American Association of State Highway and Transportation Officials, 2007.
[18] ISO 13918:2018+A1:2021 Welding. Studs and ceramic ferrules for arc stud welding, 2018.
[19] ISO 6892–1:2019 Metallic materials. Tensile testing. Method of test at room temperature, 2019.
[20] Afshan S, Rossi B, Gardner L. Strength enhancements in cold-formed structural sections — part I: material testing. J Constr Steel Res 2013;83:177–88. https://doi.org/10.1016/j.jcsr.2012.12.008.
[21] ISO 14555:2017 Welding. Arc stud welding of metallic materials, 2017.
[22] prEN 1994–1-1 (working draft) Eurocode 4-Design of composite steel and concrete structures. General rules and rules for buildings, CEN, 2023.
[23] R. L'Hermite, Idées actuelles sur la technologie du béton. La Documentation technique du batiment et des travaux publics, 1955.
[24] ANSI/AISC 360–22 Specification for Structural Steel Buildings, American Institute of Steel Construction (AISC), 2012.
[25] Standard Specifications for Steel and Composite Structures, Japan Society of Civil Engineers, 2007.
[26] AS/NZS 2327:2017 Composite structures. Composite steel-concrete construction in buildings, Standards New Zealand, 2017.
[27] CSA-S16–24 Design of steel structures, CSA Group, 2024.
[28] Hicks SJ. Design shear resistance of headed studs embedded in solid slabs and encasements. J Constr Steel Res 2017;139:339–52. https://doi.org/10.1016/j.jcsr.2017.09.018.
[29] Pallarés L, Hajjar JF. Headed steel stud anchors in composite structures, Part I: shear. J Constr Steel Res 2010;66(2):198–212. https://doi.org/10.1016/j.jcsr.2009.08.009.
[30] Rambo-Roddenberry M. Behavior and Strength of Welded Stud Shear Connectors. (PhD Thesis). Virginia Polytechnic Institute and State University,; 2002.
[31] Badie S, Tadros M, Kakish H, Splittgerber D, Baishya M. Large shear studs for composite action in steel bridge girders. Bridge Eng 2002;7(3):195–203. https://doi.org/10.1061/ASCE1084-070220027:3195.
[32] Lam D, El-Lobody E. Behavior of headed stud shear connectors in composite beam. J Struct Eng 2005;131(1):96–107. https://doi.org/10.1061/(ASCE)0733-9445(2005)131:1(96).
[33] Xue W, Ding M, Wang H, Luo Z. Static behavior and theoretical model of stud shear connectors. Bridge Eng 2008;13(6):623–34. https://doi.org/10.1061/ASCE1084-0702200813:6623.
[34] Bouchair A, Bujnak J, Duratna P, Lachal A. Modeling of the steel-concrete push-out test. Procedia Engineering. Elsevier Ltd,; 2012. p. 102–7. https://doi.org/10.1016/j.proeng.2012.07.063.
[35] Spremic M, Markovic Z, Veljkovic M, Budjevac D. Push-out experiments of headed shear studs in group arrangements. Adv Steel Constr 2013;9(2):139–60.
[36] Lin Z, Liu Y, He J. Behavior of stud connectors under combined shear and tension loads. Eng Struct 2014;81:362–76. https://doi.org/10.1016/j.engstruct.2014.10.016.
[37] Q. Han, Y. Wang, J. Xu, and Y. Xing, "Static behavior of stud shear connectors in elastic concrete-steel composite beams," Jun. 22, 2015, Elsevier Ltd. doi: 10.1016/j.jcsr.2015.06.006.
[38] Kim J, Kwark J, Joh C, Yoo S, Lee K. Headed stud shear connector for thin ultrahigh-performance concrete bridge deck. J Constr Steel Res 2015;108:23–30. https://doi.org/10.1016/j.jcsr.2015.02.001.
[39] Xu C, Su Q, Masuya H. Static and fatigue behavior of the stud shear connector in lightweight concrete. Int J Steel Struct 2018;18(2):569–81. https://doi.org/10.1007/s13296-018-0014-1.
[40] Wang J, Qi J, Tong T, Xu Q, Xiu H. Static behavior of large stud shear connectors in steel-UHPC composite structures. Eng Struct 2019;178:534–42. https://doi.org/10.1016/j.engstruct.2018.07.058.
[41] Gao Y, Li C, Wang X, Zhou Z, Fan L, Heng J. Shear-slip behaviour of prefabricated composite shear stud connectors in composite bridges. Eng Struct 2021;240. https://doi.org/10.1016/j.engstruct.2021.112148.
[42] Hu Y, Qiu M, Chen L, Zhong R, Wang J. Experimental and analytical study of the shear strength and stiffness of studs embedded in high strength concrete. Eng Struct 2021;236. https://doi.org/10.1016/j.engstruct.2020.111792.
[43] Liu T, Nie X, Zeng J, Su H. Static and fatigue behaviors of corroded stud connectors in weathering steel–concrete composite beams. Eng Struct 2022;272. https://doi.org/10.1016/j.engstruct.2022.115030.
[44] Duan M, Zou X, Bao Y, Li G, Chen Y, Li Z. Experimental investigation of headed studs in steel-ultra-high performance concrete (UHPC) composite sections. Eng Struct 2022;270. https://doi.org/10.1016/j.engstruct.2022.114875.